This is a repository copy of *Near-wall dynamics of inertial particles in dilute turbulent channel flows*.

Near-wall dynamics of inertial particles in dilute turbulent channel flows

L. F. Mortimer [a)], D. O. Njobuenwu, and M. Fairweather

School of Chemical and Process Engineering, University of Leeds, Leeds, LS2 9JT, UK

[a)] Corresponding author: l.f.mortimer@leeds.ac.uk

This investigation considers the effect of Stokes number on the near-wall particle dynamics of two-phase (solid-fluid) turbulent channel flows. The spectral element method-based direct numerical simulation code Nek5000 is used to model the fluid phase at a shear Reynolds number, $Re_\tau = 180$. Dispersed particles are tracked using a Lagrangian approach with one-way coupling. Eulerian fluid and particle statistics are gathered and analysed to determine the effect of Stokes number, firstly on macroscopic statistics. Previous work of this nature indicates that mean streamwise particle velocities and rms velocity fluctuations are reduced in the bulk and increased very close to the wall, an effect which is stronger with increased particle Stokes number or inertial particles. This phenomenon has important consequences for mechanisms such as particle deposition and preferential concentration, and so for the first time this work aims to elucidate the dynamics of this effect through rigorous analysis on various scales. An in-depth force analysis indicates the importance of the lift force, even at increased Stokes numbers, in predicting particle motion in the buffer layer and log-law regions. It is also observed that pressure gradient and virtual mass forces are significant close to the wall. Alongside bulk velocity and acceleration statistics, microscopic behaviour is analysed by considering region-based particle dynamics. Probability density functions are used to determine the effect of Stokes number on particle motion in three near-wall regions, as well as within the bulk flow. It is observed that at higher Stokes numbers, the viscous sublayer contains particles with dynamic properties similar to those present in the buffer layer. This suggests rapid inter-layer migration in the wall direction, causing increased particle turbulence intensities in near-wall regions. A local flow topology classification method is also used to correlate particle behaviour with near-wall coherent turbulent structures, and a mechanism for particle sweep towards the wall is suggested. Finally, low-speed streak accumulation and inter-layer particle fluxes are considered and the extent of mixing for low and high Stokes numbers is discussed.

I. INTRODUCTION

Elucidating the dynamics surrounding the transport of particles within fluid flows is of great importance in understanding natural phenomena and improving industrial processes. Human lung airways (Walters and Luke, 2010), tidal currents (Wang et al., 2010) and liquid-fueled combustors (Gosman and Ioannides, 1983) are but a few cases where predicting particulate phase dynamics is vital to fully understand the behaviour of the system. Furthermore, in industrial applications, accurate prediction of particle-system interaction such as deposition rates and dispersion are imperative in the efficient design of transport processes (Soldati, 2003). The present study is of particular relevance to the nuclear industry where there exists a necessity to model

particle-laden flows such as waste slurries and reactor coolant circuits, which are often difficult to study experimentally. In all such situations, the carrier flow is most likely turbulent due to the presence of high flow-rates, and being able to predict particle-boundary interaction (e.g. turbophoresis, deposition and resuspension) is of great importance practically.

Years of study into single-phase wall-bounded turbulent flows has helped develop a good understanding of the continuous phase dynamics. Of particular interest is the categorization of ordered near-wall vortical structures, which has been studied extensively (Dritselis and Vlachos, 2008). Particles entering these regions have been observed to show a wide range of responses based on their size, density and inertia (Marchioli and Soldati, 2002). Over the last few decades, the motion of particles in isotropic and wall-bounded turbulence has been simulated to study a range of behaviours and mechanisms such as dispersion, deposition, resuspension, turbulence enhancement/attenuation and interparticle collisions. Typical attempts at performing such computations use tools such as direct numerical simulation (DNS) or large eddy simulation (LES) to predict the turbulence field, however LES is less adequate for dense flows since the two-way coupling influence on turbulence kinetic energy occurs at the unresolved scales, and so further considerations must be taken into account to model this feature (M. Kuerten, 2016). The particulate phase is usually predicted concurrently with the continuous phase using one of a range of techniques such as Eulerian methods (Février et al., 2005), point-particle approaches (Maxey and Riley, 1983) and particle-resolved or interface tracking methods (Vreman, 2016). Depending on the complexity of the problem and the computational resources available, each of these fluid and particle prediction techniques can be used in conjunction with each other for a desired level of accuracy or flow specification. For instance, the limiting factor for DNS is the Reynolds number due to computational complexities associated with increased numbers of nodes required to resolve all the relevant scales. Typical studies in wall-bounded turbulent flows hence generally consider systems with low flow rates or high viscosities (Boersma, 2011; Blackburn et al., 1996; Moser and Moin, 1984; Kim et al., 1987; Vreman and Kuerten, 2014; Lee and Moser, 2015).

Despite an increasing number of investigations into particle-laden flows, however, the physics underpinning the motion of inertial particles in these systems is yet to be fully understood. One-way coupled Lagrangian particle tracking (LPT) simulations indicate two major mechanisms which govern the dispersive properties of particle-laden flows. The first is preferential accumulation (Elghobashi and Truesdell, 1992; Squires and Eaton, 1991; Eaton and Fessler, 1994) which results in non-uniform particle distributions. The extent to which this mechanism impacts on the concentration field is governed by the Stokes number (based on the Kolmogorov scale), St_η. Experiments performed by Fessler et al. (1994) using small, dense particles in channel flows indicated the greatest response at $St_\eta \approx 1$ wherein particles would congregate in streak-like regions of low speed. However, for similar studies in homogeneous isotropic turbulence, Wood et al. (2005) observed the greatest

preferential concentration for $St_\eta = 0.6$. Another important mechanism is turbophoresis, in which particles are encouraged towards regions of low turbulence kinetic energies (Reeks, 1983). This results in accumulation of particles close to the wall and various studies have observed and quantified this phenomena (Kuerten and Vreman, 2005; Marchioli et al., 2008; Marchioli and Soldati, 2002), with the magnitude of the effect scaling with St_η. The particle transfer dynamics in the wall region are governed by the existence of coherent turbulence structures which cause heavier particles to undergo 'sweep' and 'ejection' events (Rouson and Eaton, 2001). The extent to which these migration mechanisms occur in wall-bounded flows in particular has been shown (Crowe et al., 1985) to be governed by the channel-specific particle shear Stokes number $St^+ = \tau_P/\tau_F$, which is the ratio of the particulate phase relaxation time $\tau_P = \rho_P d_P^2 / 18\rho_F \nu_F$ to the viscous flow timescale $\tau_F = \nu_F/u_\tau^2$. Here, ρ_P and ρ_F are the particle and fluid densities respectively, d_P is the particle diameter, ν_F is the fluid kinematic viscosity and u_τ is the fluid shear velocity. For very low shear Stokes numbers ($St^+ \ll 1$), particles behave as tracers and follow the fluid streamlines closely. This type of system exhibits a homogenous concentration profile, and mean particle motion statistics tend to match those of the fluid. Conversely, for very large Stokes numbers, the particle response time is much greater than that of the associated fluid timescale, so particles decouple from the turbulent fluctuations. These heavy particles migrating towards the near-wall region exhibit behaviour different to that in the bulk flow. For example, studies in channels (Li et al., 2001; Zhao et al., 2015; Rouson and Eaton, 2001) all predict increased particle turbulence intensities close to the wall for high Stokes numbers. However, they lack in explanation as to how this phenomenon arises. Likewise, certain mid-range Stokes number particles in this region are subject to local segregation and accumulation in low-speed streaks (Dritselis and Vlachos, 2008; Marchioli and Soldati, 2002; Fessler et al., 1994; Lee and Lee, 2015). Studies also indicate that particle positions in the viscous sublayer and the buffer region correlate with the local flow topology for low Stokes numbers (Soldati and Marchioli, 2009). More recent work (Sardina et al., 2012; Sardina et al., 2014) has demonstrated a strong link between the two mechanisms of wall accumulation and local clustering intensity.

Macroscopic quantities of the particle-fluid system (concentration profiles, mean velocity profiles, etc.) are directly related to the microscopic trajectories of individual particles, which are further governed by the interaction between particles and turbulent structures. Therefore, by attempting to establish a relationship between the topology of the system with reference to particle behaviour in particular regions of the flow, it is possible to build up understanding of how the macroscopic behaviour is shaped by the presence of turbulence. The majority of previous studies use Lagrangian particle tracking techniques to predict the dispersed phase, but more recently fully resolved methods have also been implemented to study channel flows with relatively low particle numbers, typically in the thousands (Uhlmann, 2005). Polydispersity was investigated using this

approach for high volume fractions, with fluid and particle statistics not significantly altered from those of the monodispersed case (Fornari et al., 2018).

The present work aims to elucidate the dynamics surrounding particle motion in each region of the turbulent channel flow, and therefore the point-solid representation will be used to study large ensembles of particles. In the literature, little explanation is offered for the existence of enhanced particle root-mean-square (rms) velocity fluctuations within the buffer layer and viscous sublayer for particles with high Stokes numbers, a phenomenon which is present in most particulate flow studies performed at around $Re_\tau = 180$, but is unexplained. This work also addresses this issue by analyzing high accuracy simulations of particle motion in those regions. Primarily, the effect of Stokes number on macroscopic system properties will be discussed. Secondly, we will focus on specific wall-normal regions of the channel and attempt to provide evidence for particle transport mechanisms. This will be established by correlating local mean particle statistics and probability density functions (PDFs) with local flow topologies, following a similar classification to that used by Blackburn et al. (1996). Furthermore, we will study Stokes numbers outside the range usually considered by previous work (obtained by varying the particle-fluid density ratio $\rho_P^* = \rho_P/\rho_F$, whilst maintaining constant particle diameter). However, consideration will also be given to the behaviour of previously studied mid-range viscous Stokes numbers ($St_\tau = 1, 5, 25$) in the form of a validation.
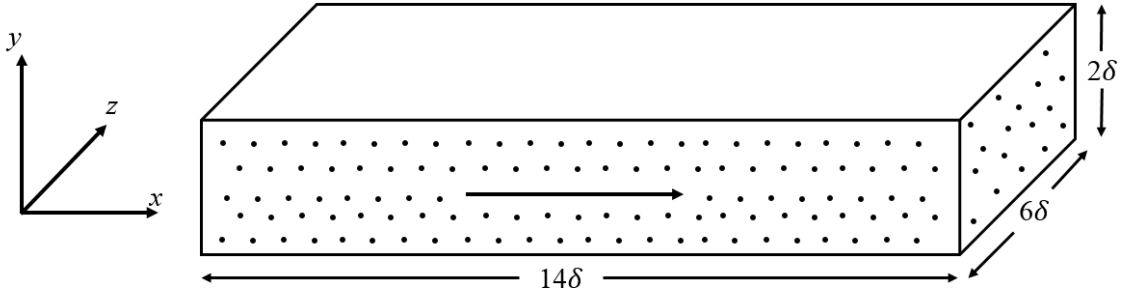
II. METHODOLOGY

A. Channel flow simulation

Due to the nature of the study, it is important to obtain a representation of the turbulent channel flow which captures all the information surrounding the smallest scales associated with the turbulent flow structure. A highly accurate flow-field is therefore acquired by utilizing direct numerical simulation, which resolves all the fine turbulence length and timescales. In this work, the Eulerian solver, Nek5000 (Fischer et al., 2008), was employed which utilizes a high-order spectral element method to simulate the fluid phase. This code was chosen due to its efficient parallelisation capabilities, high accuracy for low computational cost and extensive testing and validation history. Furthermore, the solver is open-source and provides a strong framework for developing additional components. For the continuous phase, the governing equations are the dimensionless incompressible continuity and Navier-Stokes equations, given by:

$$\boldsymbol{\nabla} \cdot \boldsymbol{u}^* = 0, \tag{1}$$

$$\frac{D\boldsymbol{u}^*}{Dt^*} = -\boldsymbol{\nabla}p^* + \frac{1}{Re_B}\nabla^2\boldsymbol{u}^* + \boldsymbol{f}_{PG}^*, \tag{2}$$

4

where $\boldsymbol{u}^*$ is the fluid velocity vector, p^* is the fluid pressure, Re_B is the bulk Reynolds number defined as $Re_B = U_B\delta/\nu_F$, ν_F is the fluid kinematic viscosity and $\boldsymbol{f}^*_{PG}$ represents the constant pressure gradient forcing term. These equations are non-dimensionalised using the channel half-height, δ, the bulk fluid velocity, U_B, and the fluid phase density, ρ_F. From here on, a quantity with an asterisk (*) denotes a variable non-dimensionalised in this manner. For this study, we consider solely the effects of the fluid on the particles (one-way coupling) and so no two-way coupling additional source term is applied. Despite simulating at a reasonably large particle volume fraction, we consider that the particles may equally be injected in an ensemble of individual identical systems. This would leave the macroscopic statistics (ensemble averages) unchanged. This allows for focus on understanding the dynamics of solely particle motion in turbulent regions without including the effects of turbulence modulation and inter-particle collisions.

FIG. 1 Schematic for multi-phase turbulent channel flow at $Re_\tau = 180$.

The governing equations are solved to high accuracy on a discretized Cartesian grid consisting of $27 \times 18 \times 23$ 7$^{\text{th}}$ order elements (i.e. 3.9M nodes). The elements are scaled such that those closest to the wall are distributed more densely. For this study, the computational position domain (x, y, z) corresponds to a $14\delta \times 2\delta \times 6\delta$ channel as presented in Fig. 1. Here, x is the streamwise direction, y is the wall-normal direction, and z is the spanwise direction. Periodic boundary conditions are enforced in the streamwise and spanwise directions, whereas the wall-normal axis uses no-slip and impermeability conditions at $y^* = \pm 1$. The flow is driven and maintained by a constant pressure gradient in the streamwise (x) direction. Using non-dimensional parameters, its magnitude is:

$$\frac{\partial p^*}{\partial x^*} = \left(\frac{Re_\tau}{Re_B}\right)^2, \tag{3}$$

where $Re_\tau = u_\tau\delta/\nu_F$ is the shear Reynolds number, which uses the shear velocity, $u_\tau = \sqrt{\tau_W/\rho_F}$, where τ_W is the mean wall shear stress. For the present study, the continuous phase parameters used for the analysis and validation grids are presented in Table 1.

TABLE 1: Parameters for DNS of turbulent channel flow. $L_{x,y,z}$ represent the cartesian lengths of the domain, $E_{x,y,z}$ are the number of elements in each direction.

Re_τ	Re_B	$L_x \times L_y \times L_z$	$E_x \times E_y \times E_z$
150 (Validation)	2100	$12\delta \times 2\delta \times 6\delta$	$27 \times 18 \times 23$
180 (Analysis)	2800	$12\delta \times 2\delta \times 6\delta$	$27 \times 18 \times 23$

B. Lagrangian particle tracking

To simulate the motion of particles through the flow-field, a Lagrangian particle tracker was developed which interfaces concurrently with Nek5000. Each element of the solid phase is represented by a small, impenetrable, undeformable computational sphere. After performing a continuous-phase timestep, the LPT solves the non-dimensional Newtonian equations of motion for each particle in order to calculate trajectories. The acceleration and velocity differential equations are derived by considering the force-balance between the particle's inertia and the fluid. For this study, we use a range of particle-fluid densities ($2.5 \leq \rho_P^* \leq 2041$) such that it is not known whether the Stokes drag term will be sufficiently more significant than other terms to make their omission valid. Previous work on this topic (Armenio and Fiorotto, 2001) suggests that for density ratios O(1), pressure gradient forces become relevant. For this reason, we have chosen to consider contributions from all hydrodynamic forces (drag, lift, virtual mass and pressure gradient). The only term neglected from the well-established Maxey-Riley equation (Maxey and Riley, 1983) is the Basset history force due to the requirement for long computation times (Daitche, 2015). Furthermore, gravitational and buoyancy forces were neglected due to the focus being on understanding the effects of turbulence on particle trajectories, and to allow comparison with previous work which exhibited increased near-wall particle velocity fluctuations. It should, however, be noted that the impact of gravity would be potentially significant in the context of real flows, which would require further investigation. Lastly, we also ignore the effects of particle rotation, assuming their angular velocity around all three axes are zero. This is justified since the expressions for lift force for both rotating and non-rotating particles are similar in regions where the lift force is of importance, such as in regions of high slip velocity (Cherukat and McLaughlin, 1994). The particle equations of motion are as follows:

$$\frac{\partial \boldsymbol{x}_P^*}{\partial t^*} = \boldsymbol{u}_P^* \tag{4}$$

$$\frac{\partial \boldsymbol{u}_P^*}{\partial t^*} = \frac{1}{M_{VM}} \left[\underbrace{\frac{3C_D|\boldsymbol{u}_s^*|}{4d_p^*\rho_P^*}\boldsymbol{u}_s^*}_{\text{Drag}} + \underbrace{\frac{3}{4}\frac{C_L}{\rho_P^*}(\boldsymbol{u}_s^* \times \boldsymbol{\omega}_F^*)}_{\text{Lift}} + \underbrace{\frac{1}{2\rho_P^*}\frac{D'\boldsymbol{u}_F^*}{Dt^*}}_{\text{Virtual Mass}} + \underbrace{\frac{1}{\rho_P^*}\frac{D\boldsymbol{u}_F^*}{Dt^*}}_{\text{Pressure Gradient}} \right] \tag{5}$$

6

In Eqs. (4) and (5), x_P^* represents the coordinates of the particle position, u_P^* is the particle velocity, u_F^* is the fluid velocity at the position of the particle, $u_S^* = u_F^* - u_P^*$ is the particle-fluid slip velocity, d_P^* is the diameter of the particle non-dimensionalised by the channel half-height, ρ_P^* is the particle-fluid density ratio and ω_F^* is the fluid vorticity at the particle position given by $\omega_F^* = \nabla \times u_F^*$. The drag coefficient, C_D, is taken from observations of Schiller and Naumann (1933) , such that $C_D = 24 f_D/Re_P$, where $f_D = (1 + 0.15 Re_P^{0.687})$ when $Re_P > 0.5$ and $f_D = 24/Re_P$ otherwise (in the Stokes regime). Re_P is the particle Reynolds number and is given by $Re_P = Re_B d_P^* |u_S^*|$. The expression for shear lift force uses the Saffman-Mei (Saffman, 1965; Mei, 1992) coefficient, which contains corrections to the standard Saffman coefficient for a broader range of particle Reynolds numbers. This is accurate for particle Reynolds numbers $Re_P < 100$, the variation of which is illustrated in Mei (1992). Arcen et al. (2006) investigated the influence of wall-corrected drag and lift forces but concluded that the introduction of more sophisticated expressions for these corrections is unnecessary providing the particle-wall collisions are elastic and there is an absence of gravity. The derivative $D'/Dt^* = \partial/\partial t + u_P^* \cdot \nabla$ represents the acceleration of the fluid as observed by the particle, and D/Dt^* is the standard material derivative with respect to the moving fluid. It should be noted here that using the standard material derivative for the added mass term was investigated (as is sometimes used in previous work), with negligible effect on mean force statistics. M_{VM} is an added mass modification term given by $M_{VM} = (1 + \frac{1}{2\rho_P^*})$, which is equivalent to 1 for simulations not using the virtual mass force.

Particle motion was calculated upon completion of a fluid timestep. First, the fluid velocity (and derivative) fields are spectrally interpolated using the element solution onto the position of each particle. A fourth-order accuracy Runge-Kutta scheme is then applied (with a Δt^* equal to that of the continuous phase solver) for integration of Eqs. (4) and (5) to obtain each particle's position and velocity at each fluid timestep. Particle-wall interactions used elastic collision conditions such that the particle wall-normal velocity was reversed upon reaching the boundary. In the periodic directions (streamwise and spanwise), particles exiting the boundary are reinjected to the corresponding location at the other side of the domain, matching the periodic nature of the fluid simulation.

For each particle set considered in this study, a sample size of 300,000 particles was simulated concurrently to ensure efficient averaging of statistics. Each of these sets was categorized by their corresponding Stokes number. This is a measure of the particle timescale to the corresponding fluid timescale, viscous or bulk. For instance, the shear or viscous Stokes number is given by $St^+ = \tau_P^+ = \tau_P/\tau_{Fv}$. Here, τ_P is the particle relaxation time, given by $\tau_P = \rho_P^* d_P^2/18\mu_F$, and τ_{Fv} is the fluid viscous timescale, given by $\tau_{Fv} = \nu_F/u_\tau^2$. The bulk Stokes number, $St_B = \tau_P^*$, is non-dimensionalised similarly, but uses the bulk fluid

timescale, $\tau_{FB} = \delta/U_B$. Both of these numbers characterize the non-dimensional relaxation time for a particle with respect to either the bulk or shear fluid timescales.

Particle-laden turbulent channel flows at both $Re_\tau = 150$ and $Re_\tau = 180$ were simulated for this study, the former being used as a multi-phase validation and the latter being used for the focused analysis. The properties used in each simulation are presented in Tables 2 and 3. Here, $d_P^+ = d_P u_\tau/\nu_F$, which is the diameter of the particle in wall units and $\Delta t^+ = \Delta t u_\tau^2/\nu_F$ is the timestep in wall units.

TABLE 2: Particle phase parameters for validation simulation at $Re_\tau = 150$.

Parameter	St$^+ \approx 1$	St$^+ \approx 5$	St$^+ \approx 25$
Particle diameter, d_P^*	0.001	0.002	0.005
Particle diameter, d_P^+	0.15	0.3	0.75
Number of particles, N_P	300,000	300,000	300,000
Shear Stokes number, St^+	1.000	4.998	25.010
Bulk Stokes number, St_B	0.093	0.467	2.334
Density ratio, ρ_P^*	769	769	769
Volume fraction, Θ_P	10^{-6}	10^{-5}	10^{-4}
Particle and fluid timestep, Δt*	0.01	0.01	0.01
Particle and fluid timestep, Δt$^+$	0.12	0.12	0.12

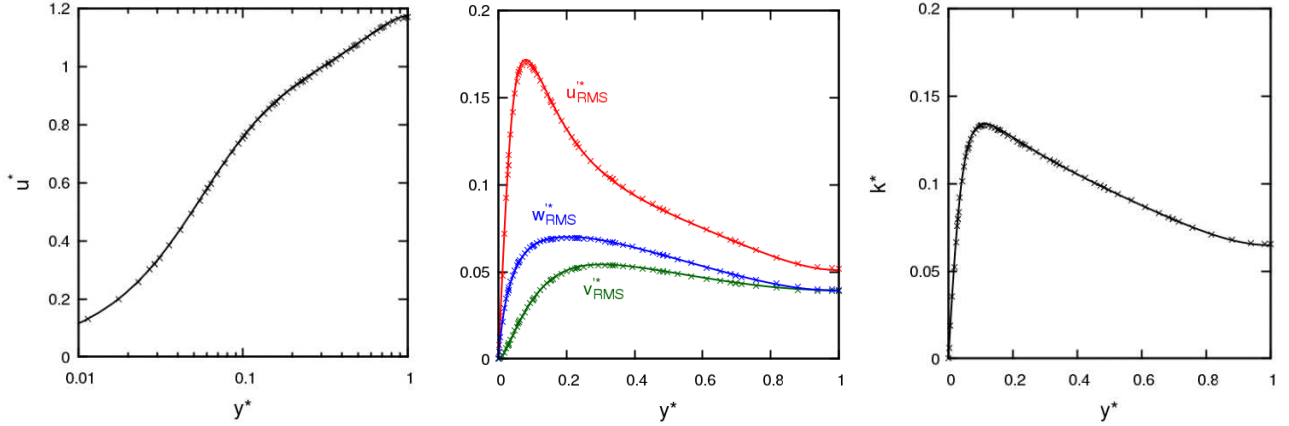**TABLE 3:** Particle phase parameters for simulation at $Re_\tau = 180$.

Parameter	St$^+ \approx 0.1$	St$^+ \approx 50$	St$^+ \approx 92$
Particle diameter, d_P^*	0.005	0.005	0.005
Particle diameter, d_P^+	0.9	0.9	0.9
Number of particles, N_P	300,000	300,000	300,000
Shear Stokes number, St^+	0.113	49.995	91.845
Bulk Stokes number, St_B	0.01	4.321	7.937
Density ratio, ρ_P^*	2.5	1111	2041
Volume fraction, Θ_P	10^{-4}	10^{-4}	10^{-4}
Particle and fluid timestep, Δt*	0.02	0.02	0.02
Particle and fluid timestep, Δt$^+$	0.23	0.23	0.23

Each simulation presented here was performed initially as a single-phase flow using an initial flow-field consisting of a turbulent mean profile with added chaotic terms in the wall-normal and spanwise directions. Once turbulence was established, fluid statistics were monitored until the mean streamwise velocity and rms velocity fluctuations had reached a statistically steady state. Particles were then injected randomly throughout the channel between $y^* = 0.1$ and $y^* = 1.9$, and given an initial velocity equal to that of the fluid at the injection position.

III. RESULTS AND DISCUSSION

A. Continuous phase validation

We begin by ensuring that the discretizations chosen for the continuous phase grid are sufficient to predict a fluid flow field with similar accuracy to previous DNS cases. The single-phase predictions for the present study at $Re_\tau = 180$ are compared to previous DNS results (Vreman and Kuerten, 2014) in Fig. 2.
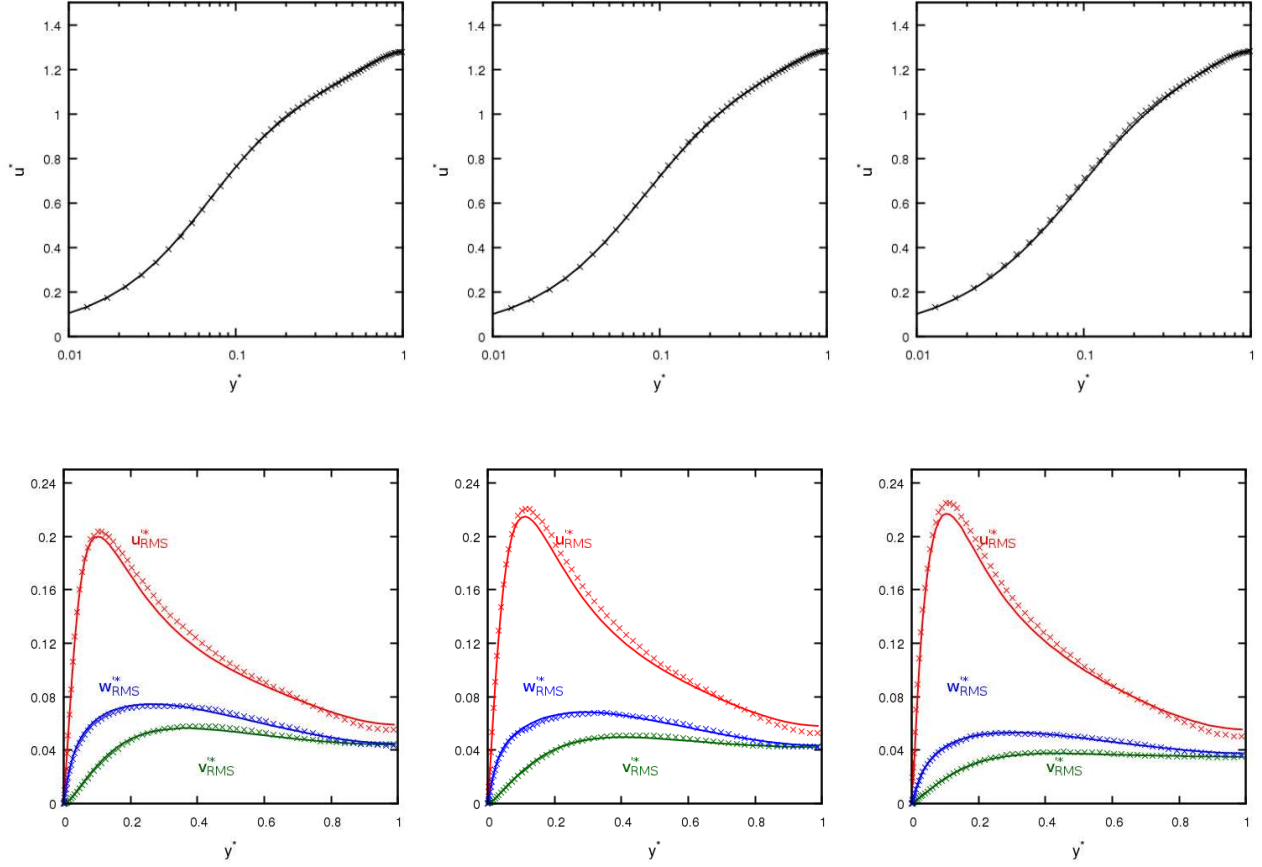

FIG. 2 DNS validation at $Re_\tau = 180$. Profiles of mean streamwise velocity (a), root mean square of velocity fluctuations (b), and mean turbulence kinetic energy (c) in turbulent channel flow. Present work (crosses) and Vremen and Kuerten (2014) (solid line) are compared.

The mean streamwise velocity of the fully developed turbulent channel flow in each simulation is first compared, and shows excellent agreement. Similar comparisons can be made for the rms of the velocity fluctuations and the mean turbulence kinetic energy. The only region where there is very slight disagreement is at the peak of the streamwise rms velocity fluctuations, however the validation predictions were taken from a database comparing a variety of DNS implementations where the strongest deviation between methods was observed in this region. Despite this, a near-perfect agreement indicates that the present flow-field can be used with confidence.

B. Discrete phase validation

To validate the particle solver, a separate simulation was performed using the same mesh for the fluid, this time at $Re_\tau = 150$. The change in Reynolds number was chosen to be able to compare directly with a database which was the result of work by Marchioli et al. (2008). Their work compared a variety of computational methods to simulate particle-laden turbulent channel flows, but solely drag forces were used when calculating particle trajectories.
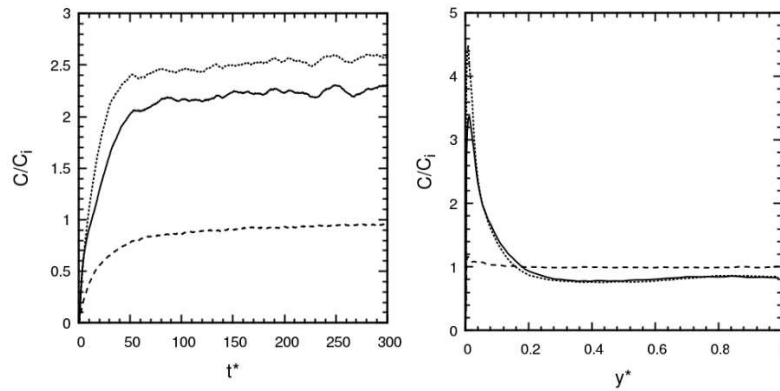
9

FIG. 3 LPT validation at $Re_\tau = 150$. Profiles of mean streamwise velocity (upper) and rms of velocity fluctuations (lower), for $St_\tau = 1$ (left), $St_\tau = 5$ (middle) and $St_\tau = 25$ (right), present work (crosses) and TUE group from Marchioli et al. (2008) (solid line) are compared

Here, the dispersed phase statistics from the TUE dataset (Marchioli et al., 2008) for particles with shear Stokes numbers $St_\tau = 1$, 5 and 25 are compared with those obtained using the present solver. The same particle parameters and forces are used in both cases and each system is one-way coupled. From Fig. 3, the mean streamwise velocity profiles show very good agreement for all three Stokes numbers. The rms velocity profiles also show very good agreement in the wall-normal and spanwise directions, but there are some slight overpredictions (near-wall) and underpredictions (bulk region) for the streamwise direction. However, this quantity had high spread of values between the simulations considered in the database, and so some deviation is to be expected. Overall, the agreement is very good and builds confidence in the results obtained at the higher Reynolds number.

C. Macroscopic particle behaviour

This section explores the effect of Stokes number on the macroscopic particle behaviour by studying first and second order particle statistics in the wall-normal direction across the width of the channel. For the present study, three different Stokes numbers are simulated, which are obtained by choosing a fixed particle diameter ($d_P^* = 0.005$) whilst varying the density ratio,
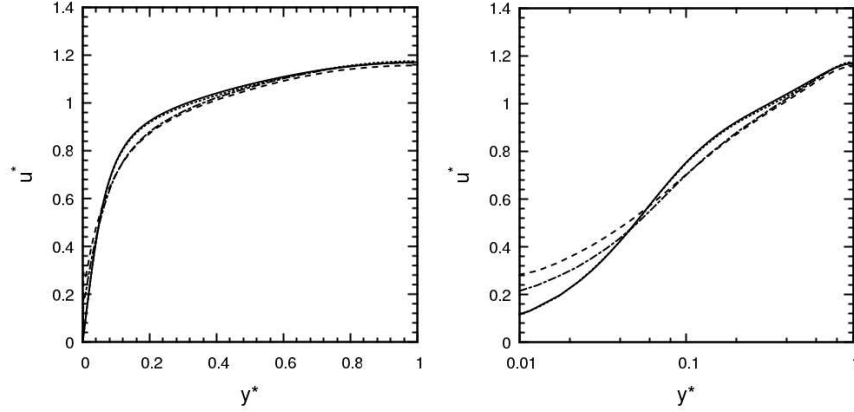
10

ρ_P^*. These have been chosen not only such that they lie beyond the boundaries of previous typical investigations, but also such that their properties match real-world systems of interest. At $St^+ = 0.1$, the analogous system is 100 μm diameter glass particles in water, with $St^+ = 92$ representing 100 μm glass particles in air. The final value of $St^+ = 50$ is chosen at the approximate mid-point between the other values considered. Each of these corresponds to the case of a real $\delta = 0.02$m channel flow. Simulations were monitored to observe whether a statistically steady state had been reached before mean statistics began being sampled. To illustrate this transition, Fig. 4 demonstrates the evolution of near-wall particle concentration over time, which was monitored for each particle set. To generate this quantity, the number of particles at position $y^* < 0.1$ was recorded each timestep and divided by the volume of the enclosed regions to generate a concentration C. This was then divided by the mean initial concentration measured across the entire channel after injection, C_i, to obtain a relative concentration. It is observed here that even the statistically steady state had a very slight constant drift of particles towards the wall, but the particle flux (or the time derivative of concentration) remained stable. The right-hand plot in Fig. 4 depicts the mean concentration profile across the channel, with statistics gathered after $t^* > 100$. It is apparent from this plot that the maximum near-wall concentration was actually obtained from the $St^+ = 50$ particle set, which agrees with the observations of Sardina et al. (2014) in boundary layers who observed maximum turbophoretic drift for particles with shear Stokes numbers between $10 \leq St^+ \leq 30$. This is explicable by the tendency for particles at this Stokes number to accumulate in elongated streamwise regions of low speed present in such flows (Pedinotti et al., 1992), which will be illustrated later. Inertial particles entering these regions will slow down, reducing the rate at which they return to the outer layer. The near-wall concentration effects associated with long-term turbophoresis have been observed previously (Arcen et al., 2006; Marchioli et al., 2008; Zhao et al., 2015)

FIG. 4 Temporal evolution of near-wall particle concentration normalised by the initial bulk concentration after injection (left) and particle concentration normalised by initial bulk concentration across the channel (right). Solid line: $St^+ = 92$; dotted: $St^+ = 50$; dashed: $St^+ = 0.1$.

To obtain these, the channel domain was divided across the wall-normal direction into 128 regions, with endpoints given by the following equation: $s_f^i = -\cos(\pi i/128)$, ensuring thinner regions in the areas of greater turbulence and eventual

particle concentration. Each timestep, averages of quantities presented below were calculated and updated for each region. Figure 5 compares the mean streamwise velocity profiles (non-dimensionalised using the bulk flow velocity, U_B) of each particle set with that of the unladen fluid.
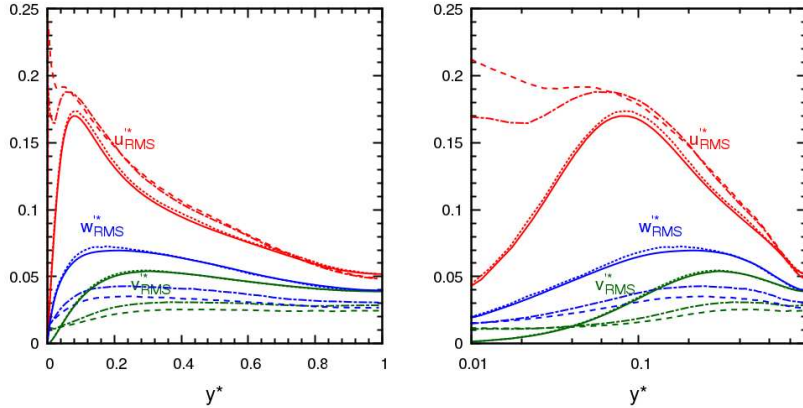

FIG. 5 Comparison of mean streamwise particle velocity profiles. Solid line: unladen flow; dashed: $St^+ = 92$; dot-dashed: $St^+ = 50$; dotted: $St^+ = 0.1$. The right-hand graph is plotted on a logarithmic scale.

As expected, the $St^+ = 0.1$ particles follow the fluid streamlines very closely and act as tracers. As the Stokes number (or in this case, density ratio) increases, the deviation increases such that heavier particles in the bulk and log-law regions lag behind the fluid, whilst particles in the viscous sublayer and buffer layer overtake the fluid. This behaviour is known (Picciotto et al., 2005), but the mechanisms responsible remain unclear. Close to the wall, these results indicate that the particle inertia is high enough in these regions to maintain speeds larger than those of the fluid, but the question remains as to how particles enter these regions whilst retaining their velocities. Evidently, there are two competing mechanisms at play which equalize at $y^* \approx$ 0.05. As the channel centreline is approached, the inertial particles are unable to keep up with the fluid which is likely due to turbophoretic drift towards the channel centreline from particles which originally approached the wall but did not reach the positive-gradient turbulence kinetic energy region (see Fig. 2c). These wall-normal transport mechanisms shall be a primary focus of the analysis later on in the paper.
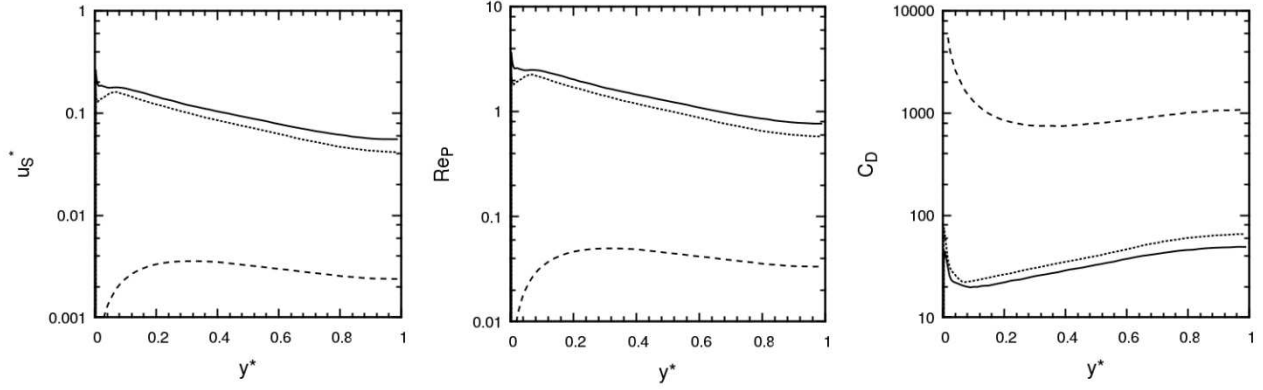
The rms velocity fluctuations for both the unladen fluid and each particle set are presented in Fig. 6. Here, we observe a similar tracer effect at $St^+ = 0.1$, although there are slight deviations in the turbulent region. At higher Stokes numbers, the spanwise and wall-normal components are dampened when compared to the unladen flow. This effect is most apparent in the turbulent region and scales with Stokes number. Conversely, the streamwise rms profiles are greatly enhanced everywhere aside from at the central plane of the channel, and this effect is strongest near the wall boundary. The fact that these rms profiles do not go to zero at the wall is an interesting feature which is only exhibited at very high Stokes numbers. In previous work (Zhao et al., 2015), it is suggested that this phenomenon is due to wall-collisions and large particle-fluid momentum transfer.

However, near-wall particles subject to sudden wall-normal velocity direction changes would have very little effect on the resulting statistics, since intensity is based on speed as opposed to direction. Also, the present work shows particles exhibiting this behaviour under a one-way coupled regime. The remaining analysis focuses on better understanding this phenomenon and we shall provide reasons for this effect in the remaining discussions.
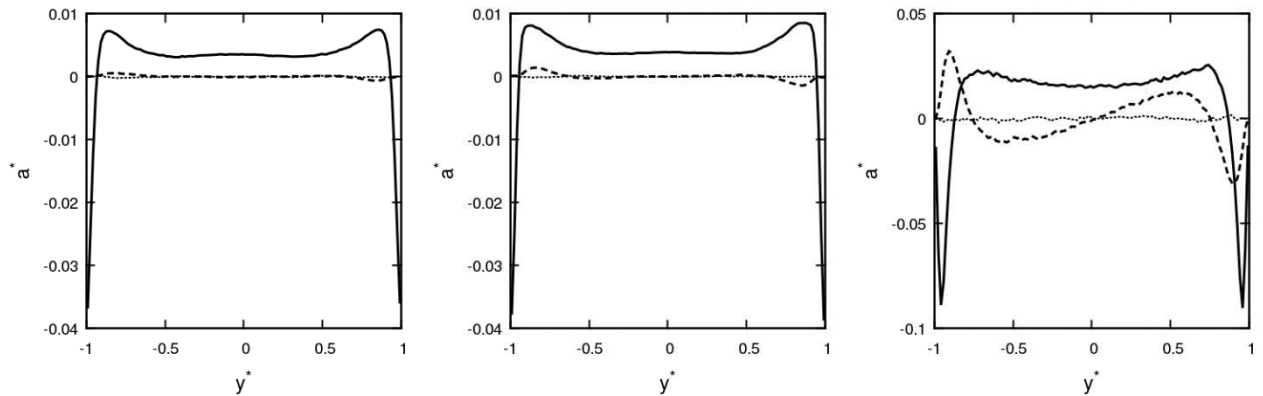

FIG. 6 Comparison of mean particle rms velocity fluctuation profiles. Solid line: unladen flow; dashed: $St^+ = 92$; dot-dashed: $St^+ = 50$; dotted: $St^+ = 0.1$. The right-hand graph is plotted on a logarithmic scale.

Other particle properties of interest which help ascertain the dynamics particles are being subjected to in each region of the flow are the slip velocity, the particle Reynolds number, and the calculated drag coefficient. Each of these is plotted across the wall-normal axis of the channel for all three Stokes numbers in Fig. 7. Slip velocities and the particle Reynolds numbers are directly related and therefore exhibit the same qualitative behaviour. They both can be used to measure the extent to which the particles follow the fluid. For instance, large slip velocities indicate decorrelation between the particle and fluid velocity fields which has a direct impact on the drag force imparted on the particle. It is observed that for $St^+ = 0.1$, these quantities are very small throughout, indicating tracer-like behaviour. They fall off to zero close to the wall, but peak between the turbulent region and the bulk flow. Because the drag coefficient is inversely proportional to the particle Reynolds number, very close to the wall this quantity is very large. For the two higher Stokes numbers, the slip velocity and particle Reynolds number exhibit a steady increase as the wall is approached, indicating maximum decoupling from the fluid in the turbulent region. In these cases, the drag coefficient remains relatively steady (between 10 and 100) throughout the domain, where its maxima located at the channel centreline and at the wall. These results are in qualitative agreement with the work of Zhao et al. (2012), but those authors only considered Stokes drag in the particle force-balance equation, and performed at a slightly lower Reynolds number, $Re_\tau = 150$.
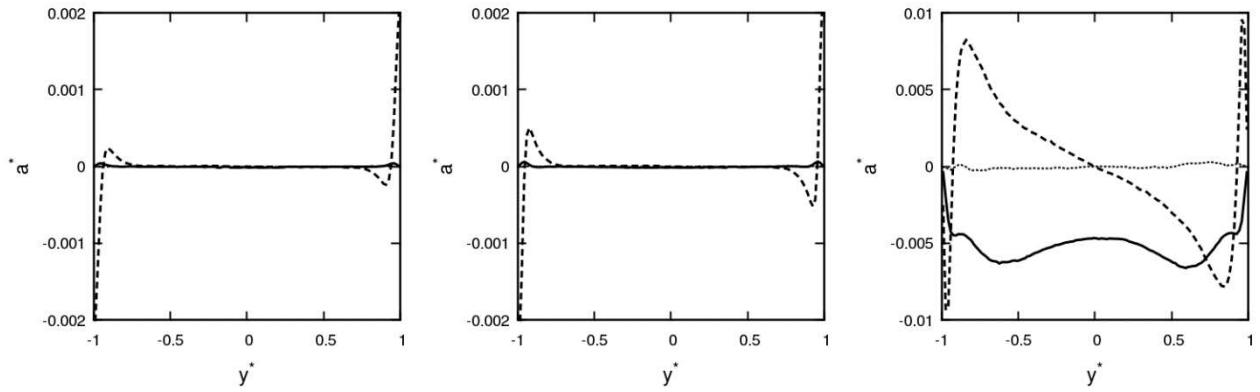
FIG. 7 Comparison of profiles of mean particle slip velocity (left), particle Reynolds number (middle) and drag coefficient (right). Solid line: $St^+ = 92$; dotted: $St^+ = 50$; dashed: $St^+ = 0.1$.

The contributions to acceleration from drag and lift in Eq. (5) are plotted in Figs. 8 and 9, respectively, for each particle Stokes number. Note that from hereon, with any quantity plotted across the entire domain, we define the walls to be at $y^* = -1$ and $y^* = 1$ such that the centreline lies at $y^* = 0$. The streamwise drag force at $St^+ = 0.1$ is homogeneous in the bulk of the channel. In the turbulent region, the magnitude peaks and the force is negative. The wall-normal drag force varies across the channel. In the bulk, the particles are carried away towards the turbulent region. A pair of stable fixed points in the wall-normal force plot is observed at $y^* = \pm 0.7$. Away from these points, the particles are subject to large forces in all directions aside from spanwise, which is a result of chaotic fluid velocities in that region. The mean spanwise forces are negligible due to the homogeneity associated with that direction. The trends observed when moving to the inertial Stokes number are due to both: (i) the inverse scaling of all force terms with density ratio, which is low for tracer-like particles and hence the forces are much greater; (ii) increased response to wall-normal turbulent fluctuations of the velocity field, in that tracer particles experience large wall-normal force contributions from the shear forces such as lift.
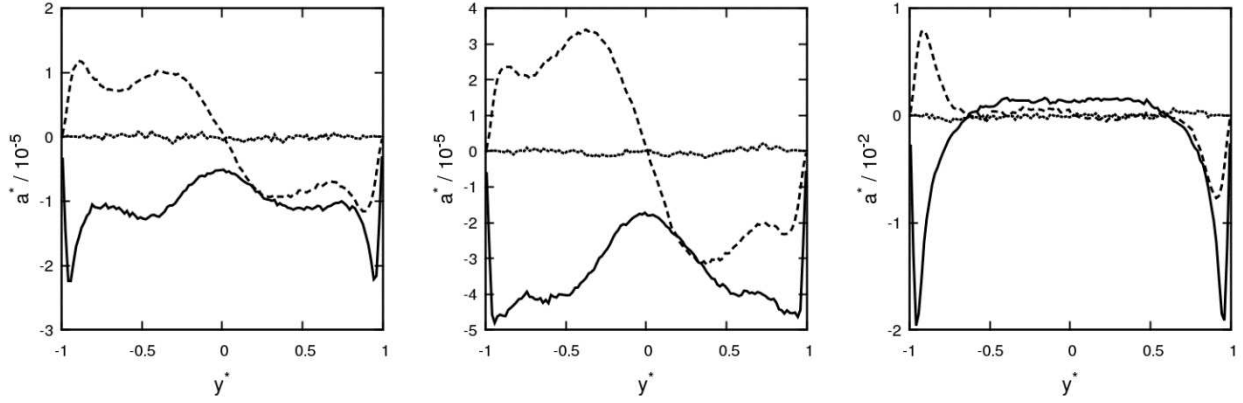

FIG. 8 Mean non-dimensionalized drag force components per particle across the channel at $St^+ = 92$ (left), $St^+ = 50$ (middle) and $St^+ = 0.1$ (right). Solid line: streamwise; dashed: wall-normal; dotted: spanwise.

14

Figure 8 also illustrates the average drag force per particle across the channel for the two higher Stokes numbers. In contrast with $St^+ = 0.1$, the mean accelerations are generally much lower due to the inverse scaling with the density ratio. The streamwise force now deviates even within the bulk of the flow, and the extent of the region of the channel where the particles are subject to large forces downstream is much greater. In the wall-normal direction, the force is only relevant in the turbulent region and is still small compared to the streamwise drag force. Again, this component demonstrates a slight tendency to push the particles back towards the bulk. At lower particle densities, the inclusion of the lift force significantly alters the motion of particles moving in a turbulent flow field, therefore this parameter is considered for each Stokes number in Fig. 9. In agreement with Armenio and Fiorotto (2001), the force is increasingly relevant in the wall regions, peaking in the viscous sublayer. At $St^+ = 92$ and $St^+ = 50$, the lift force is negligible when compared with drag, but becomes relevant for the $St^+ = 0.1$ particles. The streamwise component acts to decelerate the particles in the bulk, whereas the wall-normal component pushes particles back towards the bulk, and scales with distance from the centreline.
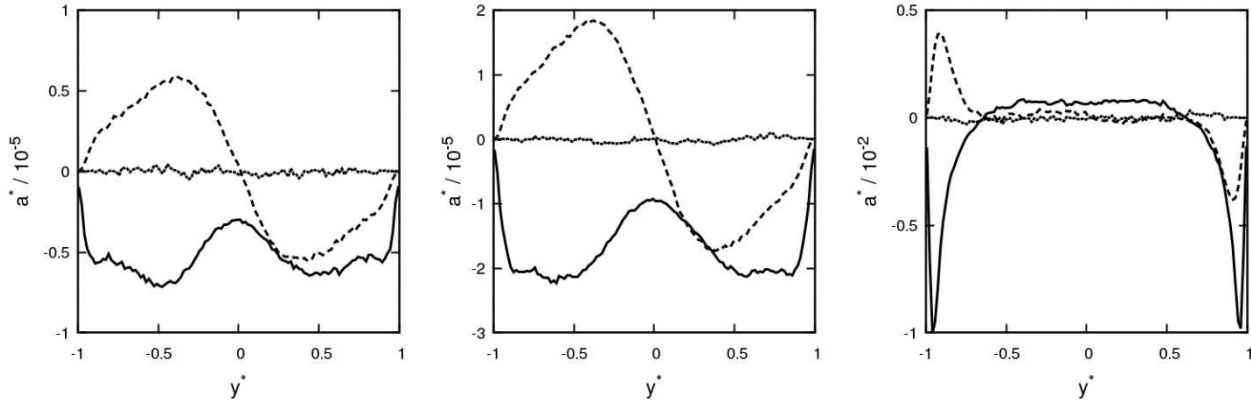

FIG. 9 Mean non-dimensionalized lift force components per particle across the channel domain at $St^+ = 92$ (left), $St^+ = 50$ (middle) and $St^+ = 0.1$ (right). Solid line: streamwise; dashed: wall-normal; dotted: spanwise.

Figures 10 and 11 illustrate the average pressure gradient and virtual mass forces across the channel. For the two higher Stokes numbers, contributions from these terms are very low when compared to the drag force (~0.1%). Due to the inverse scaling with density ratio, the contribution from these terms becomes very significant for the $St^+ = 0.1$ particles. Their magnitudes are comparable with the lift force in the near-wall region. Since $\boldsymbol{u_F} \approx \boldsymbol{u_P}$ at low Stokes numbers, the material derivatives used to calculate these terms are approximately equivalent. Hence, the only difference is a factor of two, indicated by comparing Figs. 10 and 11 for the $St^+ = 0.1$ particle set. Here, both of these forces act to accelerate particles in the bulk, and decelerate particles in the near-wall regions. Their wall-normal components also act to reintroduce particles from the wall regions back into the outer layer.
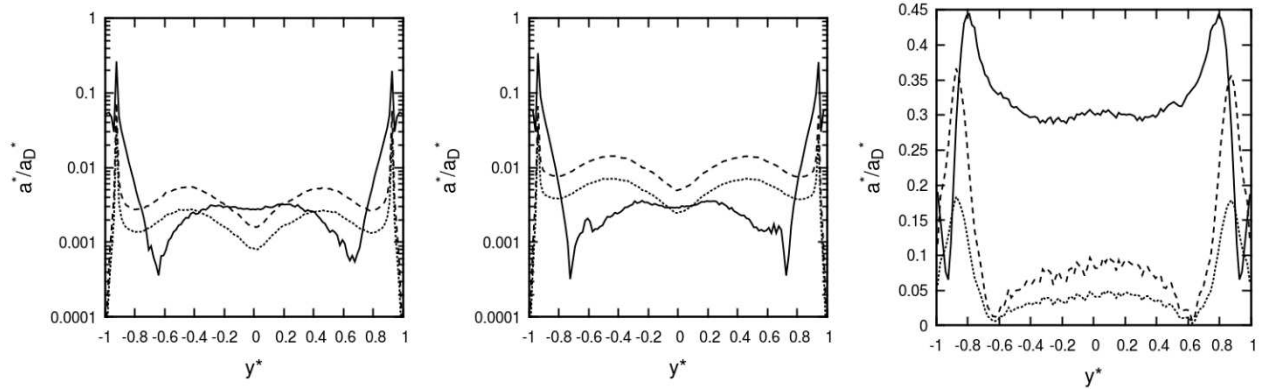
15

FIG. 10 Mean non-dimensionalized pressure gradient force components per particle across the channel domain at $St^+ = 92$ (left), $St^+ = 50$ (middle) and $St^+ = 0.1$ (right). Solid line: streamwise; dashed: wall-normal; dotted: spanwise.

FIG. 11 Mean non-dimensionalized virtual mass force components per particle across the channel domain at $St^+ = 92$ (left), $St^+ = 50$ (middle) and $St^+ = 0.1$ (right). Solid line: streamwise; dashed: wall-normal; dotted: spanwise.

To determine the importance of the various forces at each of the Stokes numbers studied, Fig. 12 illustrates the magnitude of each component normalized by the corresponding drag contribution across the height of the channel. At $St^+ = 0.1$, the lift force is greatest in the log-law region and peaks at around 45% of the drag force, reinforcing the necessity for taking into account such term for low Stokes number particles. Even in the bulk, the lift force is around 30% of the drag force. Interestingly, the pressure gradient and virtual mass forces also exhibit considerable magnitudes in the buffer layer, peaking at 36% and 18% of the drag force respectively. These findings imply that all three of these forces are likely to play a vital role in the particle dynamics which take place in the near-wall regions, with contributions to the overall acceleration vector on the same order of magnitude as the drag component. We do, however, observe that drag is the dominant force (in terms of overall magnitude) at all regions in the channel. As the Stokes number is increased, the magnitudes of all forces become negligible relative to the drag force in the bulk region, with pressure gradient and virtual mass terms only contributing around O(1%) of the drag force at $St^+ = 50$, and O(0.1%) for $St^+ = 92$. We again see the lift force exhibiting slight contribution in the buffer layer, peaking at

around 30% at $St^+ = 50$ and 25% for the $St^+ = 92$ particles. The pressure gradient and virtual mass forces also exhibit peaks in this region, but in all cases are below 10% of the drag force.

FIG. 12 Mean force magnitude relative to the drag force magnitude across the channel domain at $St^+ = 92$ (left), $St^+ = 50$ (middle) and $St^+ = 0.1$ (right). Solid line: lift; dashed: pressure gradient; dotted: virtual mass.

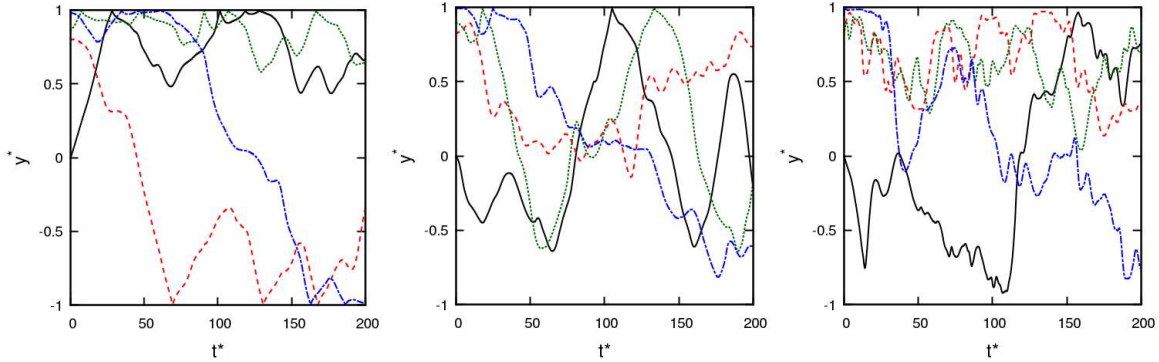### D. Region-based particle dynamics

This section focuses on identifying the key particle dynamics associated with each layer of the turbulent channel flow. The four layers considered are presented in Table 4. Here, $y^* = -1$ represents the lower wall of the channel, and each region is mirrored about the channel centerline at $y^* = 0$. When henceforth referring to the wall region, we consider the zone encompassing the viscous sublayer through to (and inclusive of) the log-law region.

TABLE 4: Turbulent channel flow at $Re_\tau = 180$ region definitions.

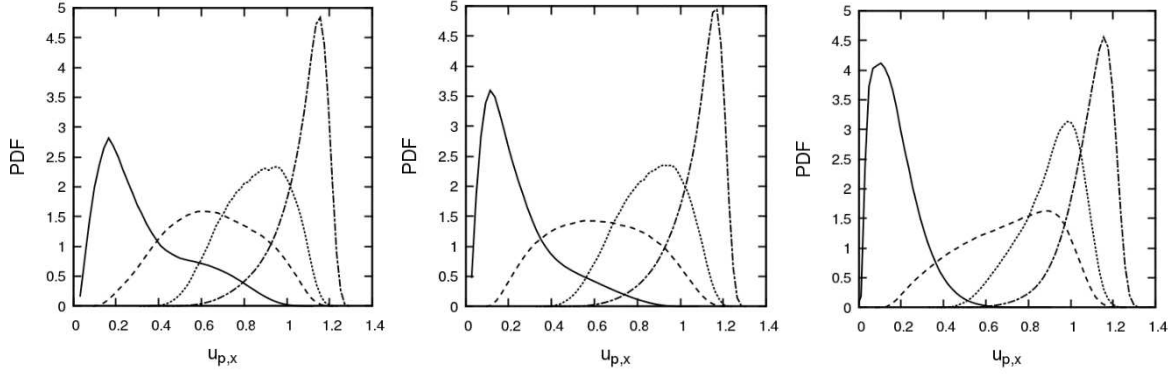| Region	Start (y*)	End (y*)	Start (y⁺)	End (y⁺)
Viscous sublayer	-1.000	-0.973	0	5
Buffer layer	-0.973	-0.834	5	30
Log-law region	-0.834	-0.800	30	36
Bulk flow	-0.800	0.000	36	180

Sample trajectories in the wall-normal direction for particles released from each of these locations are depicted in Fig. 13. These plots help determine the microscopic motion of single particles, and aid in visualizing the differences associated with particles of low and high inertia. For instance, it is indicated visually that particles at $St^+ = 92$ exhibit more wall collisions than those at $St^+ = 50$. Furthermore, the $St^+ = 0.1$ particles sampled indicate no wall collisions at all. There also seems to be a broad trend in that the particle with higher Stokes numbers change their wall-normal direction much less frequently than those with lower values. For $St^+ = 92$, wall collisions tend to account for most of the changes in direction. The qualitative predictions of particle trajectories in turbulent channel flows presented by Li and Ahmadi (1992) indicate similar dispersive properties for all

17

the particle Stokes number they studied, however, they were restricted to a very small range of particle sizes (below $5\mu m$) and as such the results presented here indicate much more varied behaviour at increased Stokes numbers.

FIG. 13 Particle trajectories in the wall-normal direction for particles released in different regions at $St^+ = 92$ (left), $St^+ = 50$ (middle) and $St^+ = 0.1$ (right). Solid line: viscous sublayer; dashed: buffer layer; dotted: log-law region; dot-dashed: bulk flow.
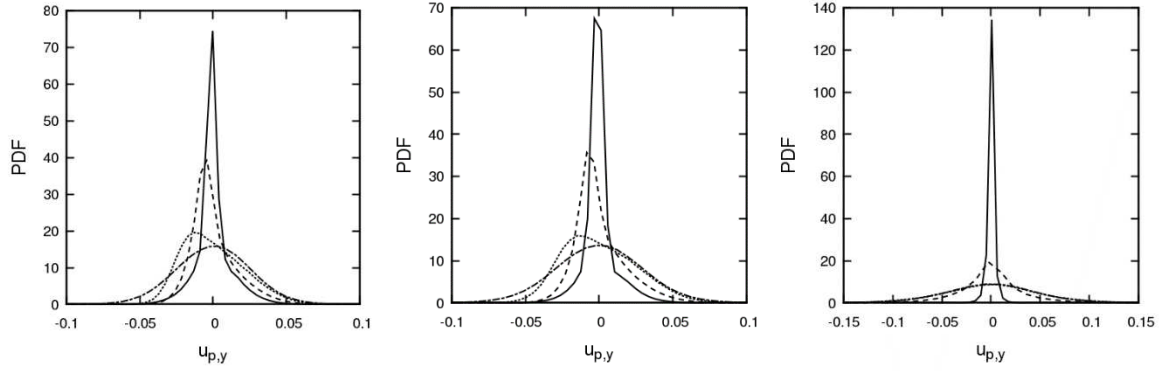
Probability density functions of various dynamic quantities were gathered for each region to obtain more information surrounding local behaviour. This will later be correlated with the flow topology for each layer. Figure 14 shows the streamwise particle velocity PDFs in each region for all three Stokes numbers. It is evident in all cases that as the channel centre is approached, the mean value of the distribution of velocity increases. It is also apparent that the bulk distribution is very similar for all three Stokes numbers. Comparing with Fig. 5, this confirms a homogeneity of particle behaviour towards the centreline, independent of Stokes number, and particularly for streamwise motion. A feature of interest occurs for the $St^+ = 92$ case, where there appears to be a secondary distribution of streamwise velocities in the viscous sublayer around $u_{p,x} = 0.6$. This indicates two regimes of particle motion in the viscous sublayer. The fact that the secondary peak matches the distribution in the buffer layer could indicate fast transfer of particles from that region, where particles do not have enough time to lose their momenta upon entering the viscous sublayer. This supports the observations of Fig. 5 which indicate particles moving faster than the fluid in the near-wall regions. Mechanisms for migration in these regions involving interaction with turbulence structures will be discussed in the following subsection.
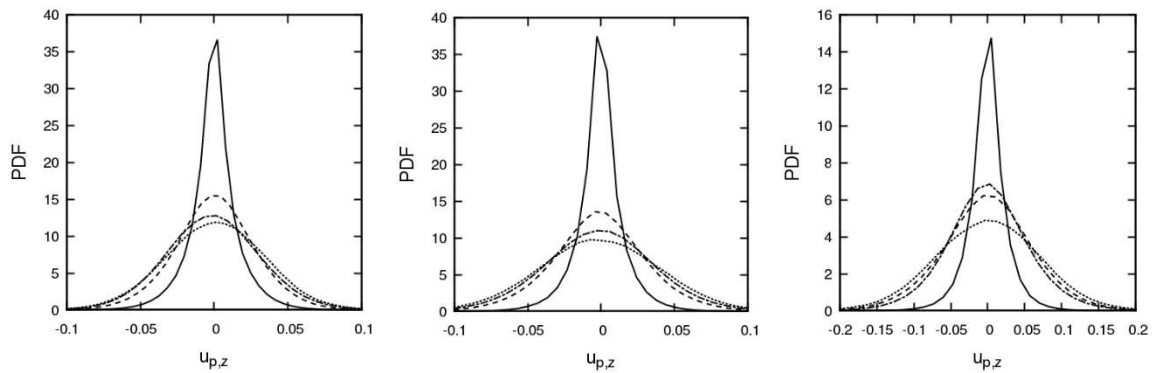
18

FIG. 14 Probability density function for the particle streamwise velocity in each region of the channel at $St^+ = 92$ (left), $St^+ = 50$ (middle) and $St^+ = 0.1$ (right). Solid line: viscous sublayer; dashed: buffer layer; dotted: log-law region; dot-dashed: bulk flow.

PDFs of wall-normal velocities in each layer are shown in Fig. 15. Aside from in the bulk, samples were only taken in the upper wall-normal region to provide more information surrounding motion towards and away from the boundary. In the case of $St^+ = 0.1$, each region has a symmetric distribution such that there are an equal number of particles with positive as negative velocities. This indicates strong homogenous mixing for tracer particles. Here, particles in the viscous sublayer have very precise wall-normal velocities, the range of which increases as they approach the bulk, which is in agreement with Fig. 6. The bulk region shows the most symmetric distribution, indicating that particles in the bulk region have their velocities travelling both towards and away from the wall in equal amounts, on average. For the higher Stokes numbers, particles have a tendency to favour negative wall-normal velocities, meaning that they are skewed towards more often travelling to the wall. As such, the interactions the particles undergo in the near-wall region cause their wall-normal motion to change, and this is most apparent in the log-law region, with the distribution becoming once again symmetric in the viscous sublayer. The symmetry in wall-normal velocity in the closest region to the wall is likely due to the wall collisions providing reversed velocities which balance with those from particles which are moving to the boundary. The widening of the particle wall-normal distributions in the near-wall regions is consistent with the findings of Sardina et al. (2012).

Fig. 16 shows region-based PDFs of the spanwise velocity for each Stokes number. Evidently, all distributions are symmetric due to the periodicity and homogeneity in that direction. As indicated by the velocity fluctuations in Fig. 6, the range of spanwise velocities increases as Stokes number decreases. Although a homogeneous direction, the spanwise motion is important since it determines the amount of time particles spend in the vicinity of spanwise turbulence structures, which can often be as wide as 15% of the channel domain (Hussain et al., 1987). These results indicate that tracer particles will sample these structures more closely in the bulk, but speed through fairly rapidly when close to the wall. Inertial particles are likely to spend more time in the vicinity of these structures, with a range of spanwise velocities almost half that of their tracer-like counterparts.

FIG. 15 Probability density function for the particle wall-normal velocity in each region of the channel at $St^+ = 92$ (left), $St^+ = 50$ (middle) and $St^+ = 0.1$ (right). Solid line: viscous sublayer; dashed: buffer layer; dotted: log-law region; dot-dashed: bulk flow.
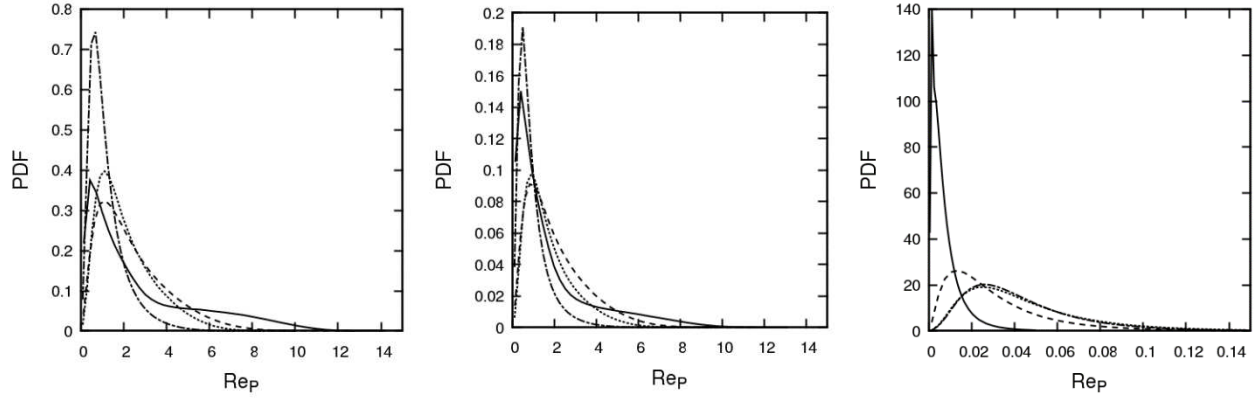

FIG. 16 Probability density function for the particle spanwise velocity in each region of the channel at $St^+ = 92$ (left), $St^+ = 50$ (middle) and $St^+ = 0.1$ (right). Solid line: viscous sublayer; dashed: buffer layer; dotted: log-law region; dot-dashed: bulk flow.
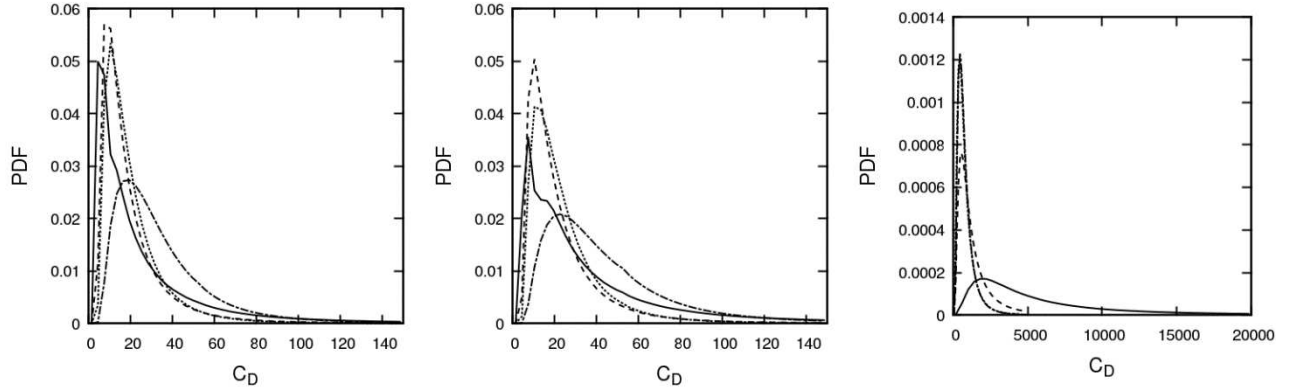
PDFs of region-based particle Reynolds number (Re_P) are presented in Fig. 17. For the two larger Stokes numbers, there is not a great difference between the layers, other than that the viscous sublayer has a larger range which seems to stretch far beyond that of the other three layers, likely due to more impactful collisions with the wall leading to further decorrelation from the fluid flow in that region and hence greater slip velocities (see Fig. 7). Conversely, for $St^+ = 0.1$, particles in the viscous sublayer have very low Reynolds numbers, which increase as the bulk is approached. This implies that particles very close to the wall have very low slip velocities and hence follow the flow almost perfectly. Due to the low turbulence and mean velocity in this region, low Stokes number particles have enough time to adjust to the surrounding velocity with ease.

Lastly, Fig. 18 illustrates the drag coefficient (C_D) distributions in each region for the three Stokes numbers. Qualitatively, the two higher Stokes number particles exhibit similar characteristics, with peaks for most regions residing around $C_D = 10$. At $St^+ = 0.1$, due to the low particle Reynolds numbers, drag coefficients are much higher, and are distributed over a much larger range. The impact on the resulting force calculations is hence that the flow field imparts very large drag forces on the tracer particles, and from Fig. 8 we observe that these are largest towards the wall. In the viscous sublayer, particles are observed

20

to possess drag coefficients greater than 10,000. From Figs. 17 and 18, it is evident that in all cases, the greatest range of particle dynamics are found within the viscous sublayer.

FIG. 17 Probability density function for the particle Reynolds number in each region of the channel at $St^+ = 92$ (left), $St^+ = 50$ (middle) and $St^+ = 0.1$ (right). Solid line: viscous sublayer; dashed: buffer layer; dotted: log-law region; dot-dashed: bulk flow.
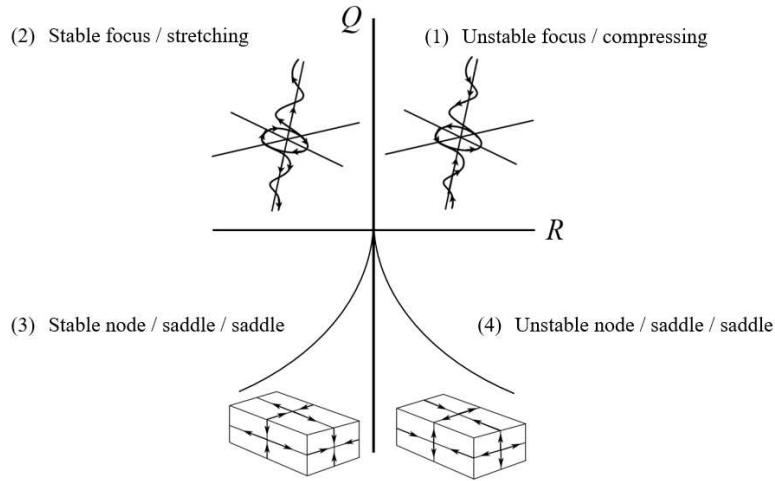

FIG. 18 Probability density function for the particle drag coefficient in each region of the channel at $St^+ = 92$ (left), $St^+ = 50$ (middle) and $St^+ = 0.1$ (right). Solid line: viscous sublayer; dashed: buffer layer; dotted: log-law region; dot-dashed: bulk flow.

E. Particle dynamics and flow topology

In this section, the behaviour of particles in each near-wall region is related to their interaction with local coherent flow structures. To classify structures within each region, we use the scheme of Blackburn et al. (1996). Using the latter approach, each fluid field point can be categorised into one of four topology types, illustrated in Fig. 19. These are (in regular quadrant ordering): unstable focus / compressing, stable focus / stretching, stable node / saddle /saddle and unstable node / saddle / saddle. Fluid points representing vortices have Q-R space points in the first two regions, and the last two regions represent convergence zones, where Q and R are, respectively, the second and third invariants of the velocity gradient tensor. The four regions identified in Section D are used to compare Q-R values computed on the fluid grid points with Q-R values computed
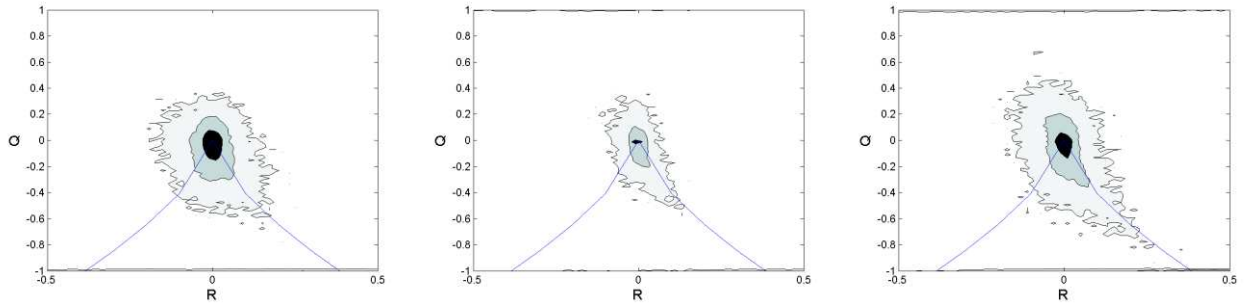
21

at particle locations for snapshots of the statistically converged simulations. Each of these calculations is illustrated as a two-dimensional PDF with contoured regions representing equivalent ranges of Q-R point density.

FIG. 19 Q and R tensor invariants for incompressible flow topology classification. Solid curved lines represent D = $(27/4)R^2 + Q^3 = 0$. After Blackburn et al. (1996), region terminology is that of Chong et al. (1990).
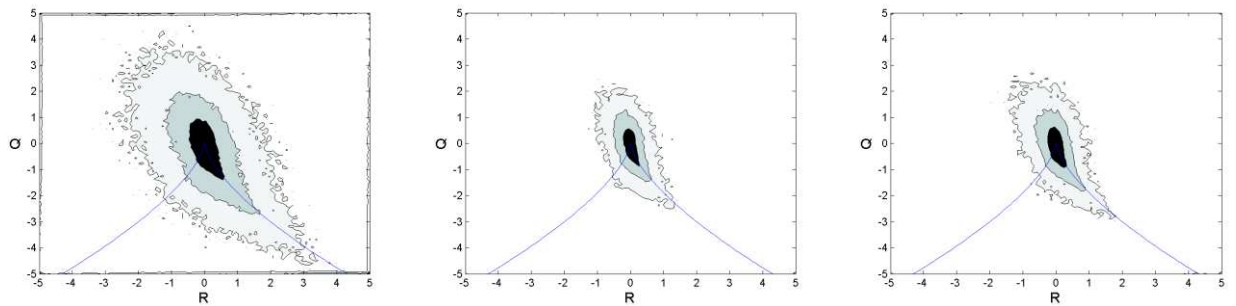
Figure 20 compares PDFs at the fluid grid points with those at particle positions for the $St^+ = 0.1$ and $St^+ = 92$ simulations, using solely points sampled from the viscous sublayer. Fluid node values indicate almost isotropy in radial preference, with a slight lean towards the fourth quadrant, which corresponds to unstable node / saddle / saddle type points. Considering particle position based sampling, both exhibit a greater preference towards the convergence zones, which are areas where particles are likely to congregate. Similar findings were observed in Rouson and Eaton (2001).

From the size of the distributions, it is clear that the inertial particles sample large magnitudes of both Q and R, favouring strong vorticity, which are avoided by the low Stokes particles. They also preferentially sample the stretching vortices and unstable node / saddle / saddle convergence zones and are completely uncorrelated with the Q-R distribution of sampled fluid nodes. These findings suggest that inertial particles entering the viscous sublayer are likely already decorrelated from the local flow velocities and as such are sampling large distributions of both Q and R, weighted towards the stretching vortices and unstable node / saddle / saddle regions, both of which are associated with turbulence structures capable of transporting particles away from the critical point.
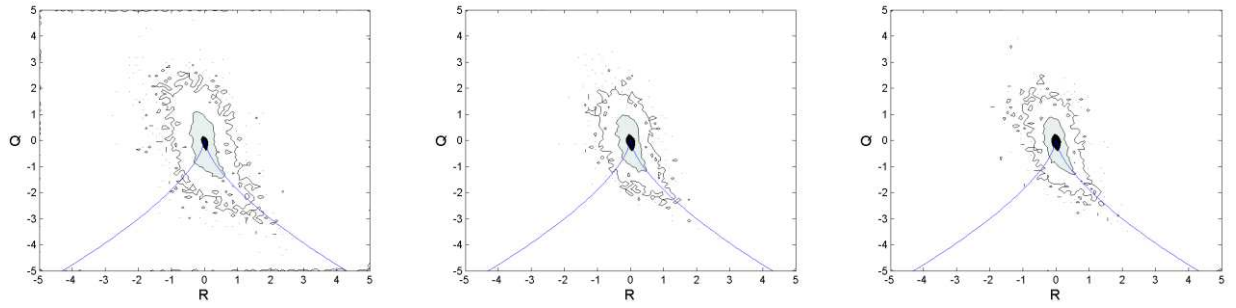
22

FIG. 20 PDF of invariants of the velocity gradient tensor, Q and R, sampled at fluid nodes and particle positions in the viscous sublayer at fluid nodes (left), and for St+ = 0.1 (middle) and St+ = 92 (right) particles.

Figure 21 illustrates the same PDFs, this time sampled in the buffer layer. Moving away from the wall, the fluid grid points now exhibit a much more pronounced preference for stable focus / stretching vortices and the unstable node / saddle / saddle topologies. Comparing the two particle sets, the $St^+ = 92$ particles sample more of the strongest stretching vortical regions than the $St^+ = 0.1$ particles, which is similar to the type of sampling occurring for the former particles in Fig. 20. The existence of these structures here, along with the preferential sampling of these structures (particularly for inertial particles), strongly indicates that an interaction is taking place which results in particles in the viscous sublayer sampling the same type of vortex classification. We believe this provides an explanation and mechanism for the buffer layer to viscous sublayer transfer phenomenon mentioned earlier since particles are ejected from these regions and yet still possess similar characteristic sampling in the viscous sublayer. Hence it appears that particles encountering stretching vortex cores are ejected in the direction of the wall.

FIG. 21 PDF of invariants of the velocity gradient tensor, Q and R, sampled at fluid nodes and particle positions in the buffer layer at fluid nodes (left), and for St+ = 0.1 (middle) and St+ = 92 (right) particles.

Figures 22 and 23 compare Q-R PDFs for the log-law region and the bulk flow. In each case, there is very little effect of Stokes number on the resulting distributions. Furthermore, the particles exhibit no obvious preferential concentration in these regions when compared to the fluid.

23

FIG. 22 PDF of invariants of the velocity gradient tensor, Q and R, sampled at fluid nodes and particle positions in the log-law region at fluid nodes (left), and for St+ = 0.1 (middle) and St+ = 92 (right) particles.
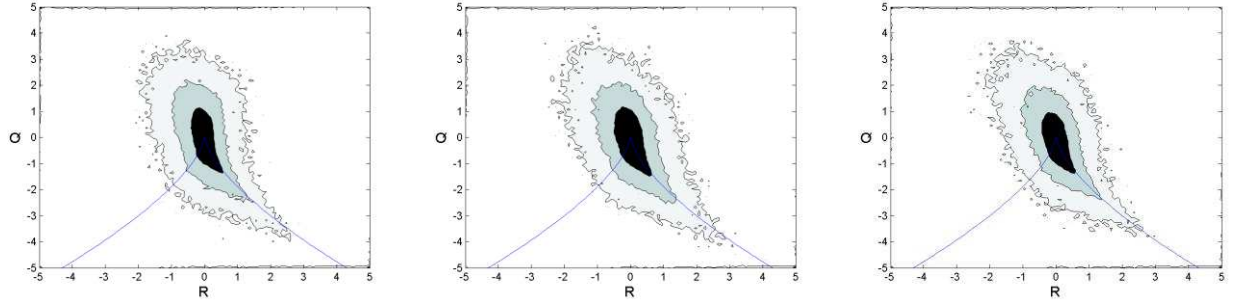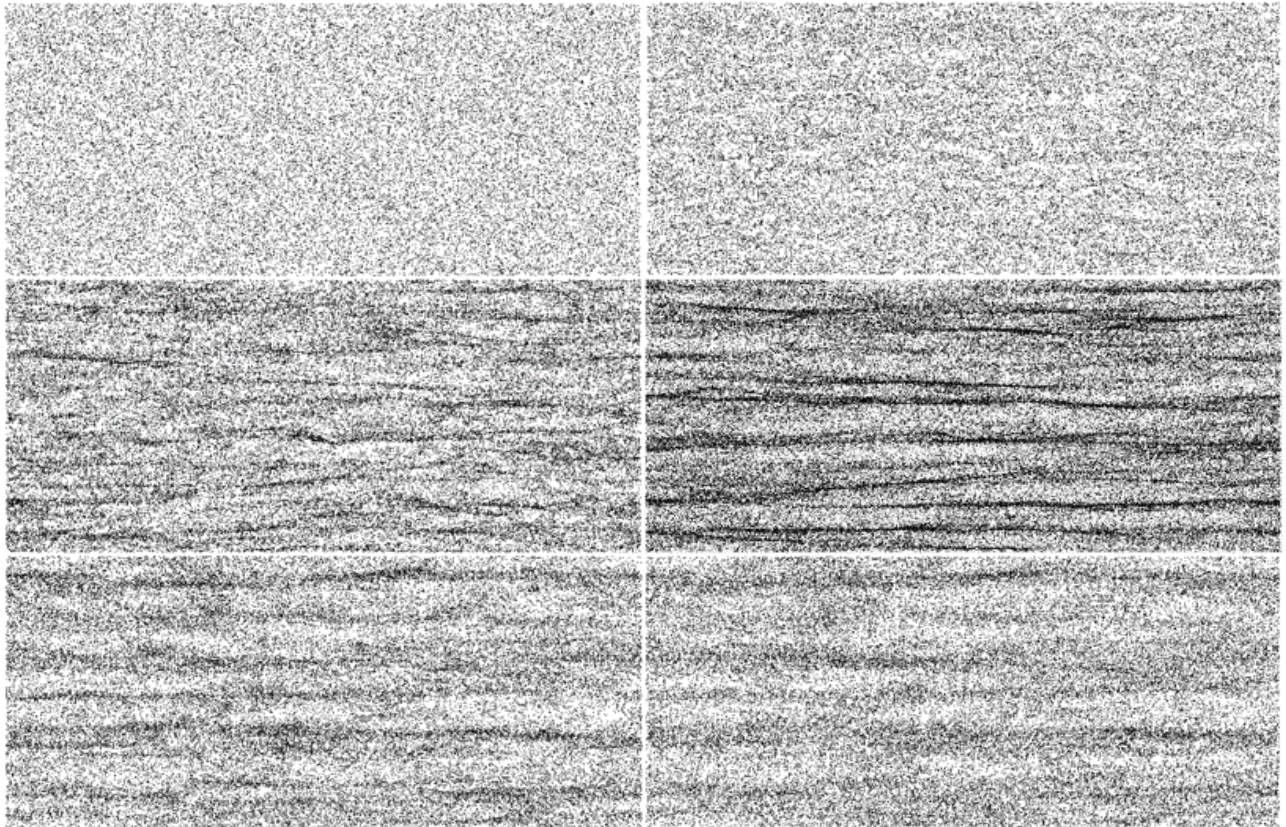

FIG. 23 PDF of invariants of the velocity gradient tensor, Q and R, sampled at fluid nodes and particle positions in the bulk flow region at fluid nodes (left), and for St+ = 0.1 (middle) and St+ = 92 (right) particles.

FIG. 24 Instantaneous near-wall particle distributions at $y^* = 0.9$ for $St^+ = 0.1$, 1, 5, 25, 50 and 92 starting at top-left and ending at lower-right (moving left to right). $St^+ = 1$, 5 and 25 were taken from the validation simulations at a slightly lower Reynolds number, $Re_\tau =$

24

150.

Instantaneous particle distributions near the channel boundary were obtained from the final timestep of each simulation and are presented in Fig. 24. Results from the validation runs have been included here to provide a more in-depth overview of the response of near-wall particle segregation to Stokes number, however, it should be emphasised that results at $St^+ = 1, 5$ and 25 were obtained at a slightly lower Reynolds number, and with an absence of lift, pressure gradient and virtual mass forces. Therefore, the extent of preferential concentration is likely to vary slightly at $Re_\tau = 180$. Despite this, the overall trend is clear; particles at very low Stokes numbers are homogenously distributed near the wall, showing very little indication of their location within low speed streaks. As the Stokes number increases, the level of order increases likewise, and the results indicate a maximum level of order by inspection at $St^+ = 25$. Above this value, the streaks begin to become much less clear, as the particles begin to decouple from the fluid motion.

TABLE 4: Inter-region mean particle fluxes.

Region	F+ ($St^+ = 0.1$)	F+ ($St^+ = 92$)	F- ($St^+ = 0.1$)	F- ($St^+ = 92$)
Bulk flow	-	-	994	449
Log-law	994	456	914	458
Buffer layer	914	463	137	576
Viscous sublayer	136	576	-	-

Lastly, to determine the effect of Stokes number on particle mixing, mean fluxes were calculated through the boundaries between each region between t* = 200 and t* = 300 to ensure the statistics were stationary. The results of this investigation are presented in Table 4. Here, F+ represents the flux towards the wall, and F- represents the flux away from the wall. It is evident that in all cases, the net flux through each plane is approximately zero, with a slight preference for turbophoresis at St$^+$ = 92. At St$^+$ = 0.1, the greatest mixing occurs between the bulk region and the log-law / buffer layer regions. Low Stokes number particles travelling from the buffer layer to the viscous sublayer are limited due to low velocities and large forces influencing them back towards the bulk. In the case of St$^+$ = 92 particles, the strongest mixing effect actually occurs between the buffer layer and the viscous sublayer. Since particles are likely ejected into this region, they reach the wall with high velocities and so elastic wall reflections likely remove particles from this region at the same rate that they enter.

IV. CONCLUSIONS AND OUTLOOK

Lagrangian particle tracking and direct numerical simulation have been used to study three sets of particles in a multi-phase turbulent channel flow at $Re_\tau = 180$ to determine the effect of Stokes number on near-wall particle dynamics. Parameters have been chosen to augment existing work in this area by performing simulations at Stokes numbers outside the range usually

considered. Furthermore, continuous-phase topology analysis techniques have been performed to correlate particle behaviour with local turbulent structures. Turbulent channel flow results obtained using the continuous phase solver, Nek5000, at a shear Reynolds number of 180 exhibited excellent agreement with those of previous high accuracy DNS studies. Furthermore, the particle simulation technique described in this paper validated very well against the work of Marchioli et al. (2008), using a separate simulation performed at $Re_\tau = 150$.

Results indicated that particles with larger Stokes numbers tend to overtake the fluid low near the wall, and lag behind the flow in the bulk flow region. Moreover, the high Stokes particles exhibit increased rms velocity fluctuations very close to the wall, implying strong decoupling from local flow velocity fields. This is in agreement with previous work both at similar and increased fluid Reynolds numbers (Li et al., 2001; Zhao et al., 2015; Rouson and Eaton, 2001). Other components of the rms velocity fluctuations were suppressed. All of these near-wall effects scale with Stokes number. Other particle properties such as slip velocities, Reynolds numbers and drag coefficients indicated large differences in mean behaviour between low and high Stokes number particles. Concentration profiles indicated rapid near-wall accumulation for the St$^+$ = 50 and St$^+$ = 92 particle sets. In all cases, the near-wall concentration reached an approximately statistically steady state after t* > 100, however, this period still exhibited a slow and uniform particle accumulation rate. Acceleration terms due to each force were analysed across the channel and the necessity for the inclusion of the lift term was confirmed for the low particle Stokes number, accounting for large wall-normal velocities pushing particles back into the bulk of the flow. This effect was observed to be greatest at the boundary between the log-law region and the bulk flow, and could explain the increased mixing effect inherent in the St$^+$ = 0.1 system. The importance of the each force relative to the drag force was investigated, which demonstrated that the lift force is very significant, particularly in the wall region for all particle Stokes numbers, but also in the bulk for St$^+$ = 0.1. Pressure gradient and virtual mass contributions were also found to be significant in the buffer and log-law regions.

Region-based particle dynamical property PDFs were obtained throughout the channel to determine local behaviour. It was observed that at large Stokes numbers, particles in the viscous sublayer seemingly exhibit two streamwise velocity regimes, the greater of which coincides with the peak of the velocity distribution in the buffer layer. This indicates that particles from the buffer layer are entering the viscous sublayer, whilst retaining their higher streamwise velocity. A consequence of this is that the streamwise rms velocity fluctuations will be greater in this region, since the velocities of the migrating particles will differ from those of the surrounding flow. Furthermore, the rapid movement of a particle into a region of low fluid streamwise velocity in turn produces a high 'slowing' drag force (see Fig. 8), which it scales with and is highly sensitive to the distance from the wall. A spread of particle velocities is therefore generated as the particle traverses this region and decelerates with the

particles closest to the wall experiencing the greatest force. This important effect has consequences for the deposition behaviour and wall accumulation of particles, but is much less pronounced for lower Stokes numbers. In the case of previous studies, which regularly use $St^+ < 25$, this effect was not observed. Other interesting results from the PDF-based analysis include increased wall-normal velocities in the viscous sublayer for higher Stokes number particles (hence increased wall collision velocities) and greater spanwise motion in the log-law region for $St^+ = 0.1$ particles (as opposed to inertial particles where it is greatest in the bulk).

The fluid topology classification scheme of (Blackburn et al., 1996) was also used to determine the types of flow structures each set of particles were likely to sample for each region. In the viscous sublayer, it was observed that high Stokes number particles were located in regions similar in vorticity to that of the fluid in the buffer layer, implying a coupling between the two layers. The evidence presented here suggests that this could provide an additional mechanism by which inertial particles migrate laterally to the viscous sublayer whilst retaining streamwise velocities similar to those present in the buffer layer. Since most flows in real-world situations possess increased turbulence than the present channel flow considered, future studies should examine the presence of these effects at increased Reynolds numbers, where the log-law region is wider and contains much larger scale sweep events.

VI. REFERENCES

Arcen, B., Tanière, A. and Oesterlé, B., "On the influence of near-wall forces in particle-laden channel flows," International Journal of Multiphase Flow **32**(12), 1326-1339 (2006).

Armenio, V. and Fiorotto, V., "The importance of the forces acting on particles in turbulent flows," Physics of Fluids **13**(8), 2437-2440 (2001).

Blackburn, H.M., Mansour, N.N. and Cantwell, B.J., "Topology of fine-scale motions in turbulent channel flow," J. Fluid Mech. **310**, 269-292 (1996).

Boersma, B.J, "Direct numerical simulation of turbulent pipe flow up to a Reynolds number of 61,000," In: Journal of Physics: Conference Series: IOP Publishing, 042045, (2011).

Cherukat, P. and McLaughlin, J.B., "The inertial lift on a rigid sphere in a linear shear flow field near a flat wall," Journal of Fluid Mechanics **263**, 1-18. (1994).

Chong, M.S., Perry, A.E. and Cantwell, B.J., "A general classification of three-dimensional flow fields," Physics of Fluids A: Fluid Dynamics **2**(5), 765-777. (1990).

Crowe, C., Gore, R. and Troutt, T., "Particle dispersion by coherent structures in free shear flows," Particulate Science and Technology **3**(3-4), 149-158. (1985).

Daitche, A., "On the role of the history force for inertial particles in turbulence," Journal of Fluid Mechanics **782**, 567-593. (2015).

Dritselis, C.D. and Vlachos, N.S., "Numerical study of educed coherent structures in the near-wall region of a particle-laden channel flow," Physics of Fluids **20**(5), 055103. (2008).

Eaton, J.K. and Fessler, J., "Preferential concentration of particles by turbulence," International Journal of Multiphase Flow **20**, 169-209. (1994).

Elghobashi, S. and Truesdell, G., "Direct simulation of particle dispersion in a decaying isotropic turbulence," Journal of Fluid Mechanics **242**, 655-700. (1992).

Fessler, J.R., Kulick, J.D. and Eaton, J.K., "Preferential concentration of heavy particles in a turbulent channel flow," Physics of Fluids **6**(11), 3742-3749. (1994).

Février, P., Simonin, O. and Squires, K.D., "Partitioning of particle velocities in gas–solid turbulent flows into a continuous field and a spatially uncorrelated random distribution: theoretical formalism and numerical study," Journal of Fluid Mechanics **533**, 1-46. (2005).

Fischer, P.F., Lottes, J.W. and Kerkemeier, S.G., Nek5000. Web page: http://nek5000.mcs.anl.gov. (2008).

Fornari, W., Picano, F. and Brandt, L., "The effect of polydispersity in a turbulent channel flow laden with finite-size particles," European Journal of Mechanics-B/Fluids **67**, 54-64. (2018).

Gosman, A.D. and Ioannides, E., "Aspects of Computer Simulation of Liquid-Fueled Combustors," Journal of Energy **7**(6), 482-490. (1983).

Hussain, A., Jeong, J. and Kim, J., "Structure of turbulent shear flows," Center for Turbulence Research Report CTR-SS1 (1987).

Kim, J., Moin, P. and Moser, R., "Turbulence statistics in fully developed channel flow at low Reynolds number," Journal of Fluid Mechanics **177**, 133-166. (1987).

Kuerten, J. and Vreman, A., "Can turbophoresis be predicted by large-eddy simulation?," Physics of Fluids **17**(1), 011701-011704. (2005).

Lee, J. and Lee, C., "Modification of particle-laden near-wall turbulence: Effect of Stokes number," Physics of Fluids **27**(2), 023303. (2015).

Lee, M. and Moser, R.D., "Direct numerical simulation of turbulent channel flow up to $Re_\tau \approx 5200$," Journal of Fluid Mechanics **774**, 395-415. (2015).

Li, A. and Ahmadi, G., "Dispersion and Deposition of Spherical Particles from Point Sources in a Turbulent Channel Flow," Aerosol Science and Technology **16**(4), 209-226. (1992).

Li, Y., McLaughlin, J.B., Kontomaris, K. and Portela, L., "Numerical simulation of particle-laden turbulent channel flow," Physics of Fluids **13**(10), 2957-2967. (2001).

M. Kuerten, J.G., "Point-Particle DNS and LES of Particle-Laden Turbulent flow - a state-of-the-art review," Flow, Turbulence and Combustion **97**(3), 689-713. (2016).

Marchioli, C. and Soldati, A., "Mechanisms for particle transfer and segregation in a turbulent boundary layer," Journal of Fluid Mechanics **468**, 283-315. (2002).

Marchioli, C., Soldati, A., Kuerten, J., Arcen, B., Taniere, A., Goldensoph, G., Squires, K., Cargnelutti, M. and Portela, L., "Statistics of particle dispersion in direct numerical simulations of wall-bounded turbulence: Results of an international collaborative benchmark test," International Journal of Multiphase Flow **34**(9), 879-893. (2008).

Maxey, M.R. and Riley, J.J., "Equation of motion for a small rigid sphere in a nonuniform flow," The Physics of Fluids **26**(4), 883-889. (1983).

Mei, R., "An approximate expression for the shear lift force on a spherical particle at finite Reynolds number," International Journal of Multiphase Flow **18**(1), 145-147. (1992).

Moser, R. and Moin, P., "Direct numerical simulation of curved turbulent channel flow," NASA Technical Memorandum **10**. (1984).

Pedinotti, S., Mariotti, G. and Banerjee, S., "Direct numerical simulation of particle behaviour in the wall region of turbulent flows in horizontal channels," International Journal of Multiphase Flow **18**(6), 927-941. (1992).

Picciotto, M., Marchioli, C., Reeks, M.W. and Soldati, A., "Statistics of velocity and preferential accumulation of micro-particles in boundary layer turbulence," Nuclear engineering and design **235**(10-12), 1239-1249. (2005).

Reeks, M., "The transport of discrete particles in inhomogeneous turbulence," Journal of aerosol science **14**(6) 729-739. (1983).

Rouson, D.W. and Eaton, J.K., "On the preferential concentration of solid particles in turbulent channel flow," Journal of Fluid Mechanics **428**, 149-169. (2001).

Saffman, P., "The lift on a small sphere in a slow shear flow," Journal of Fluid Mechanics **22**(2), 385-400. (1965).

Sardina, G., Picano, F., Schlatter, P., Brandt, L. and Casciola, C.M., "Statistics of particle accumulation in spatially developing turbulent boundary layers," Flow, Turbulence and Combustion **92**(1-2), 27-40. (2014).

Sardina, G., Schlatter, P., Brandt, L., Picano, F. and Casciola, C.M., "Wall accumulation and spatial localization in particle-laden wall flows," Journal of Fluid Mechanics **699**, 50-78. (2012).

Schiller, L. and Naumann, A., "Fundamental calculations in gravitational processing," Zeitschrift Des Vereines Deutscher Ingenieure **77**, 318-320. (1933).

Soldati, A., "Cost-efficiency analysis of a model wire-plate electrostatic precipitator via DNS based Eulerian particle transport approach," Aerosol Science Technology **37**, 171–182. (2003).

Soldati, A. and Marchioli, C., "Physics and modelling of turbulent particle deposition and entrainment: Review of a systematic study," International Journal of Multiphase Flow **35**(9), 827-839. (2009).

Squires, K.D. and Eaton, J.K., "Preferential concentration of particles by turbulence," Physics of Fluids A: Fluid Dynamics **3**(5), 1169-1178. (1991).

Uhlmann, M., "An immersed boundary method with direct forcing for the simulation of particulate flows," Journal of Computational Physics **209**(2), 448-476. (2005).

Vreman, A., "Particle-resolved direct numerical simulation of homogeneous isotropic turbulence modified by small fixed spheres," Journal of Fluid Mechanics **796**, 40-85. (2016).

Vreman, A.W. and Kuerten, J.G.M., "Comparison of direct numerical simulation databases of turbulent channel flow at $Re_\tau = 180$," Physics of Fluids **26**(1), 015102. (2014).

Walters, D.K. and Luke, W.H., "Computational Fluid Dynamics Simulations of Particle Deposition in Large-Scale, Multigenerational Lung Models," Journal of Biomechanical Engineering **133**(1), 011003-011008. (2010).

Wang, J., Shen, Y. and Guo, Y., "Seasonal circulation and influence factors of the Bohai Sea: a numerical study based on Lagrangian particle tracking method," Ocean Dynamics. **60**(6), 1581-1596. (2010).

Wood, A., Hwang, W. and Eaton, J., "Preferential concentration of particles in homogeneous and isotropic turbulence," International journal of multiphase flow **31**(10-11), 1220-1230. (2005).

Zhao, F., George, W.K. and Van Wachem, B., "Four-way coupled simulations of small particles in turbulent channel flow: The effects of particle shape and Stokes number," Physics of Fluids **27**(8), 083301. (2015).

Zhao, L., Marchioli, C. and Andersson, H., "Stokes number effects on particle slip velocity in wall-bounded turbulence and implications for dispersion models," Physics of Fluids **24**(2), 021705. (2012).